Brillouin asymmetric spatial heterodyne oceanographic lidar receiver for profiling temperature, salinity, and sound velocity

John A. Smith and Chris Hostetler
Langley Research Center, Hampton, Virginia

NASA STI Program Report Series

Since its founding, NASA has been dedicated to the advancement of aeronautics and space science. The NASA scientific and technical information (STI) program plays a key part in helping NASA maintain this important role.

The NASA STI program operates under the auspices of the Agency Chief Information Officer. It collects, organizes, provides for archiving, and disseminates NASA's STI. The NASA STI program provides access to the NTRS Registered and its public interface, the NASA Technical Reports Server, thus providing one of the largest collections of aeronautical and space science STI in the world. Results are published in both non-NASA channels and by NASA in the NASA STI Report Series, which includes the following report types:

- TECHNICAL PUBLICATION. Reports of completed research or a major significant phase of research that present the results of NASA Programs and include extensive data or theoretical analysis. Includes compilations of significant scientific and technical data and information deemed to be of continuing reference value. NASA counterpart of peer-reviewed formal professional papers but has less stringent limitations on manuscript length and extent of graphic presentations.

- TECHNICAL MEMORANDUM. Scientific and technical findings that are preliminary or of specialized interest, e.g., quick release reports, working papers, and bibliographies that contain minimal annotation. Does not contain extensive analysis.

- CONTRACTOR REPORT. Scientific and technical findings by NASA-sponsored contractors and grantees.

- CONFERENCE PUBLICATION. Collected papers from scientific and technical conferences, symposia, seminars, or other meetings sponsored or co-sponsored by NASA.

- SPECIAL PUBLICATION. Scientific, technical, or historical information from NASA programs, projects, and missions, often concerned with subjects having substantial public interest.

- TECHNICAL TRANSLATION. English-language translations of foreign scientific and technical material pertinent to NASA's mission.

Specialized services also include organizing and publishing research results, distributing specialized research announcements and feeds, providing information desk and personal search support, and enabling data exchange services.

For more information about the NASA STI program, see the following:

- Access the NASA STI program home page at http://www.sti.nasa.gov

- Help desk contact information:

https://www.sti.nasa.gov/sti-contact-form/
and select the "General" help request type.

NASA/TP–20240000673
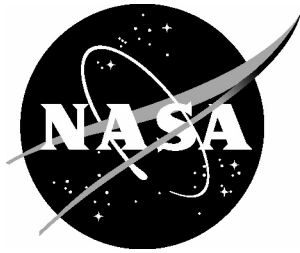
Brillouin asymmetric spatial heterodyne oceanographic lidar receiver for profiling temperature, salinity, and sound velocity

John A. Smith and Chris Hostetler
Langley Research Center, Hampton, Virginia

January 2024

1 **Brillouin asymmetric spatial heterodyne oceanographic lidar**

2 **receiver for profiling temperature, salinity, and sound velocity**

3 JOHN A. SMITH AND CHRIS HOSTETLER

4 *NASA Langley Research Center, Hampton, VA 23681, USA*

5 **john.a.smith-3@nasa.gov*

6 **Abstract:** A lidar receiver employing a proposed Brillouin asymmetric spatial

7 heterodyne (BASH) spectrometer to measure depth resolved profiles of near

8 surface ocean temperature, salinity, and sound velocity from aircraft is

9 conceptualized. A BASH spectrometer can have high throughput, can be

10 designed for any wavelength and, importantly, can be field widened, allowing

11 accurate, high spectral resolution of the Brillouin spectrum within diffuse

12 scatter from depth. Temperature and salinity are measured independently with

13 no assumptions about one or the other and the measurements are unbiased by

14 the presence of particulate or elastic scatter. A sensitivity analysis and lidar

15 simulations show the expected performance.

16 **1. Introduction**

17 No sensor today is capable of remotely sensing temperature and salinity at

18 depth. Existing techniques depend on infrared or microwave emissions that

19 originate from only the very surface (<1 mm) of the water, whereas lidars with

20 blue-green wavelength transmitters (450-550 nm) are capable of penetrating

21 10's of meters into the water. Light interacts with water by the Brillouin

(Brillouin-Mandelstam) scatter process, and by analyzing the spectrum of Brillouin scatter from a water body the temperature and salinity can be determined. For a pulsed laser source, temporally range gating the backscatter signal can provide depth resolution. There are a host of scientific and operational drivers for such a sensor, from improved hurricane and red tide forecasting to studies of ocean fronts, eddies, and freshwater lenses. Though the idea of using Brillouin scatter to measure physical properties of the ocean has been around for several decades, no fieldable sensor has been demonstrated. The challenge has been to spectrally resolve the features of the Brillouin spectrum well enough in the diffuse backscatter from water to permit an accurate and precise retrieval. A variety of methods have been explored by several groups to accomplish this. They include the use Faraday anomalous dispersion optical filters [1], Fabry-Perot interferometers [2-6], and iodine and barium vapor cells [4,7]. Vapor cells can achieve a large etendue, but they do not fully resolve the Brillouin spectrum. The Fabry-Perot interferometer and close cousin, the virtually imaged phased array (VIPA), resolves the spectrum well enough to determine both the Brillouin shift and linewidth, and therefore both temperature and salinity, but have a very limited etendue. Approaches have been studied that exploit the temperature and salinity dependence of the spectrum of Raman scatter, but their measurement performance is inherently limited during daytime due to the large spectral bandwidth of the Raman return (30-40 nm). A rugged and fieldable Brillouin lidar sensor concept is presented

44   here that combines the etendue advantages of atomic and molecular vapor

45   filters with the spectral resolution advantage of interferometric approaches,

46   overcoming a major limitation of existing approaches.

47   A variation on the original Doppler asymmetric spatial heterodyne (DASH)

48   technique – here referred to as the Brillouin asymmetric spatial heterodyne

49   ("BASH") technique – is presented. The original, Doppler variant has been used

50   to resolve Doppler shifts in airglow to measure winds in the upper atmosphere

51   [8,9]. Spatial heterodyne techniques have not previously been prescribed for

52   use in a Brillouin lidar, to this author's knowledge, but do have advantages for

53   this application. For example, the BASH technique can be implemented using

54   field widened (or field "compensated") interferometers. Since scatter from

55   depths in the ocean is diffuse, like airglow, this is a distinct advantage. The

56   BASH technique also provides enough spectral information to infer Brillouin

57   shift, Brillouin linewidth and the presence of elastic scatter unambiguously,

58   without requiring assumptions on any of these three variables. The polarizing

59   BASH variant presented here can offer very high light throughput and can be

60   designed for any wavelength that efficiently penetrates water. Spatial

61   heterodyne interferometers are also rugged and have heritage with other

62   instruments. For example, a DASH called MIGHTI flew on NASA's ICON

63   spacecraft [10], and a Michelson interferometer that shares structural

64   similarities to the DASH has flown in the 355 nm receiver channel of NASA

65   Langley Research Center's HSRL-2 airborne high spectral resolution lidar to

66 make high spectral resolution measurements of aerosols and clouds on many

67 campaigns focused on atmospheric science [11-14].

68 **2. Description of BASH technique and application to resolving Brillouin**

69 **spectrum**

70 Here, we describe the use of the novel polarizing BASH technique for resolving

71 the spectrum of Brillouin backscatter to determine the temperature, salinity, and

72 sound velocity within a water volume. The polarizing BASH technique is

73 implemented using an interferometer that is a close cousin of the polarizing

74 Michelson interferometer, but with the end mirrors replaced with gratings tilted

75 near Littrow (Fig. 1). The tilted gratings provide a spatial representation of the

76 Fourier transform of the input spectrum at the output, much like a monolithic

77 Fourier transform spectrometer. This polarizing interferometer does not reflect

78 light back to the source, and therefore has twice the throughput of a non-

79 polarizing interferometer. The polarizing DASH was introduced in [15], and

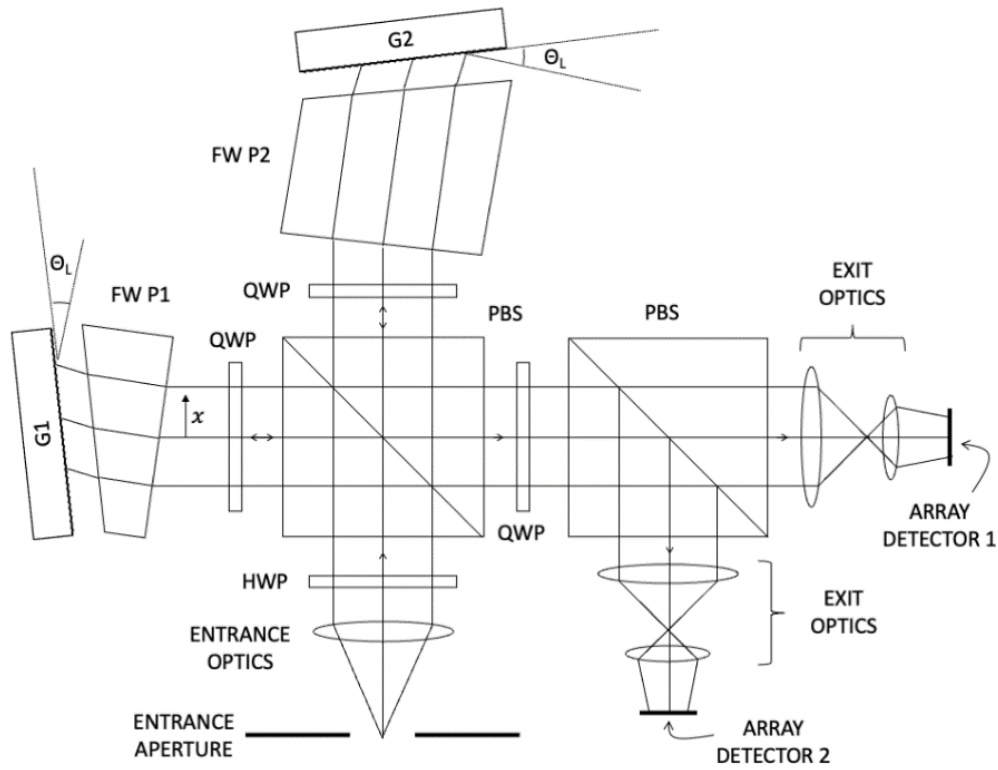80 the polarizing BASH inherits from this design.

81

Fig. 1. Illustration of dual output polarizing interferometer
implementing BASH technique. HWP: half waveplate, QWP:
quarter waveplate, PBS: polarizing beam splitter, FW P1 and
FW P2: field widening prisms, G1 and G2: gratings.

Light entering the entrance aperture is linearly polarized in the vertical
direction. After passing through the half waveplate, the polarization is rotated
45 degrees such that the subsequent polarizing beam splitter provides a 50:50
split. The light in each arm passes through field widening prisms that reduce
the sensitivity of the optical path difference (OPD) between the arms to the off-
axis angle, thereby enhancing the field of view. The gratings are tilted at near

92   the Littrow angle to create a resolvable spatial heterodyne across an OPD range

93   spanning many wavelengths (10^4-10^5). Upon passing twice through the quarter

94   waveplate, the polarization is rotated 90 degrees from its original orientation

95   and the light is directed toward the second polarizing beam splitter without

96   returning towards the source. A quarter waveplate between the first and second

97   polarizing beam splitters is oriented such that the two polarizations from each

98   arm interfere. Having experienced a change in phase from a difference in the

99   optical paths between the two arms, the interfered beams have a new linear

100   polarization with a rotation that depends on the precise phase difference

101   between them. Changes in polarization rotation are detected as changes in the

102   split ratio of the second polarizing beam splitter. The second polarizing beam

103   splitter therefore creates two, complementary interferograms. Each

104   interferogram is imaged onto its respective array detector. For light entering the

105   entrance aperture with a spectral distribution $f(v)$, the background-subtracted

106   interferograms acquired by the two array detectors can be modeled as follows.

$$I_1(x)$$

$$= \eta_1 E_0 \frac{a_1}{2} \left(1 \right.$$

$$\left. + M_1 \int_0^\infty f(v) \cos(2\pi(v - v_L)(4x \tan\theta_L + 2\Delta d)/c)\, dv \right) \qquad (1)$$

$$I_2(x)$$

$$= \eta_2 E_0 \frac{a_2}{2} \Bigg(1$$

(2)

$$- M_2 \int_0^\infty f(v) \cos(2\pi(v - v_L)(4x \tan \theta_L + 2\Delta d)/c) \, dv \Bigg)$$

107   Coefficients a_1, a_2, M_1 and M_2 parameterize defects in the interferometer

108   and are unity for a perfect interferometer with a well collimated input (field

109   widening will be treated later). M_1 and M_2 are referred to here as "visibility

110   factors." η_1 and η_2 are the photon detection efficiencies of the array detectors

111   and E_0 is proportional to the input irradiance. x is a linear position along the

112   grating aperture in the plane of Fig. 1, which maps to a linear position along the

113   detector arrays, with $x = 0$ being the center. The factor $4x \tan \theta_L + 2\Delta d$ is the

114   OPD and v_L is the Littrow frequency. The spectral distribution of the input is

115   approximated as a convolution of the laser transmitter spectrum (f_l) centered

116   on its carrier frequency (v_0) with a pair of Lorentz (Cauchy) distributions

117   centered about $v_0 + v_B$ and $v_0 - v_B$ representing the Brillouin doublet plus a

118   central Dirac delta function at v_0 representing the residual elastic scatter, as

119   shown in Eq. (3). γ is the ratio of elastic scatter to Brillouin scatter incident on

120   the BASH and v_B and Γ_B are the Brillouin shift and linewidth (FWHM),

121   respectively.

$$f(\nu) =$$

$$f_l(\nu - \nu_0) \otimes \left\{ \frac{1}{1+\gamma} \frac{1}{\pi \Gamma_B} \left[\frac{1}{1 + \left(\frac{\nu - \nu_0 + \nu_B}{\Gamma_B/2} \right)^2} \right.\right. \tag{3}$$

$$\left.\left. + \frac{1}{1 + \left(\frac{\nu - \nu_0 - \nu_B}{\Gamma_B/2} \right)^2} \right] + \frac{\gamma}{1+\gamma} \delta_\nu(\nu - \nu_0) \right\}$$
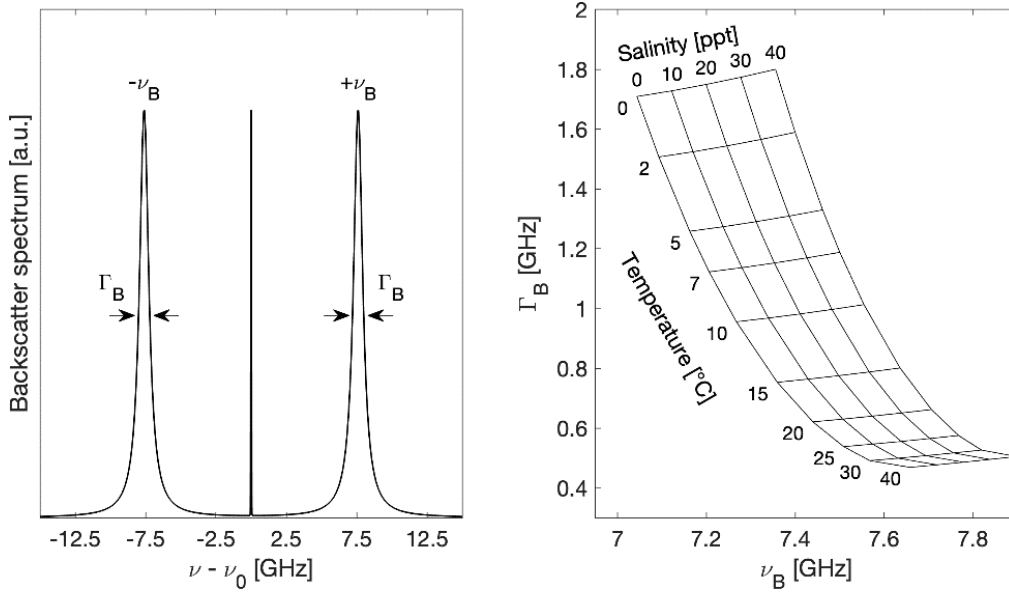
122   The Brillouin shift and Brillouin linewidth relate to the optical and physical

123   properties of the water by Eq. (4) and Eq. (5), which pertain to a backscatter

124   geometry.

$$\nu_B = \frac{2}{\lambda/n_{sw}} V_S \tag{4}$$

$$\Gamma_B \cong 8\pi \left(\frac{1}{\lambda/n_{sw}} \right)^2 \frac{1}{\rho} \left(\frac{4}{3} \eta_s + \eta_b \right) \tag{5}$$

125   Rayleigh scatter is ignored here, as it has a very small cross section

126   compared to Brillouin scatter. Also ignored is a very small dependence on

127   pressure. Note that the index of refraction of seawater (n_{sw}), sound velocity

128   (V_S), bulk viscosity (η_b), shear viscosity (η_s) and density (ρ) are all temperature

129   and salinity dependent. In this work, the index of refraction of seawater derives

130   from [16], the sound velocity and seawater density derive from [17], the bulk

131   viscosity derives from [18], and the shear (dynamic) viscosity derives from

132   [19]. There is an additional term in Eq. (5) that depends on the thermal

133   conductivity and the specific heats at constant volume and constant pressure,

134   but it is about two orders of magnitude smaller than the terms that depend on

135   the bulk and shear viscosities and so is omitted here. By these sources and Eq.

136   (4) and Eq. (5), the Brillouin shift and linewidth map to a unique temperature

137   and salinity (Fig. 2). Ppt indicates parts per thousand or g/kg (‰).

138

139   Fig. 2. Illustration of Brillouin doublet centered on elastic scatter

140   peak (left) and mapping of Brillouin shift and FWHM linewidth

141   to temperature and salinity (right) for 532 nm illumination.

142   Making the convenient substitutions $4x \tan \theta_L + 2\Delta d \rightarrow \delta$, δ now referring

143   to the optical path difference (OPD), and $\nu \rightarrow \nu' + \nu_0$, then inserting Eq. (3)

144   into Eqs. (1) and (2) and performing the integration over ν', the results are

$$I_1(\delta) = \eta_1 N_A \frac{a_1}{2} \Bigg(1 \tag{6}$$

$$+ M_1{}'(\delta) \Bigg(\frac{1}{1+\gamma} \exp\left(-\frac{\pi \Gamma_B \delta}{c} \right) \cos\left(\frac{2\pi \nu_B \delta}{c} \right)$$

$$+ \frac{\gamma}{1+\gamma} \Bigg) \cos\left(\frac{2\pi(\nu_L - \nu_0)\delta}{c} \right) \Bigg)$$

$$I_2(\delta) = \eta_2 N_A \frac{a_2}{2} \Bigg(1 \tag{7}$$

$$- M_2{}'(\delta) \Bigg(\frac{1}{1+\gamma} \exp\left(-\frac{\pi \Gamma_B \delta}{c} \right) \cos\left(\frac{2\pi \nu_B \delta}{c} \right)$$

$$+ \frac{\gamma}{1+\gamma} \Bigg) \cos\left(\frac{2\pi(\nu_L - \nu_0)\delta}{c} \right) \Bigg)$$

145    $M_1{}'(\delta)$ and $M_2{}'(\delta)$ are the visibility factors modified by the effects of a

146   transmitter with a non-zero spectral width. The last cosine factor is a heterodyne

147   between the Littrow frequency and the laser's carrier frequency and has a

148   spatial period of $c/|\nu_L - \nu_0|$. Critically, the Brillouin shift and Brillouin

149   linewidth information is encoded in the amplitude "envelope" of this Littrow

150   heterodyne, as shown in Fig. 3. This contrasts with the traditional DASH

151   technique in which the information (i.e., Doppler shift) is encoded in the phase

152   of the Littrow heterodyne rather than its amplitude.

153
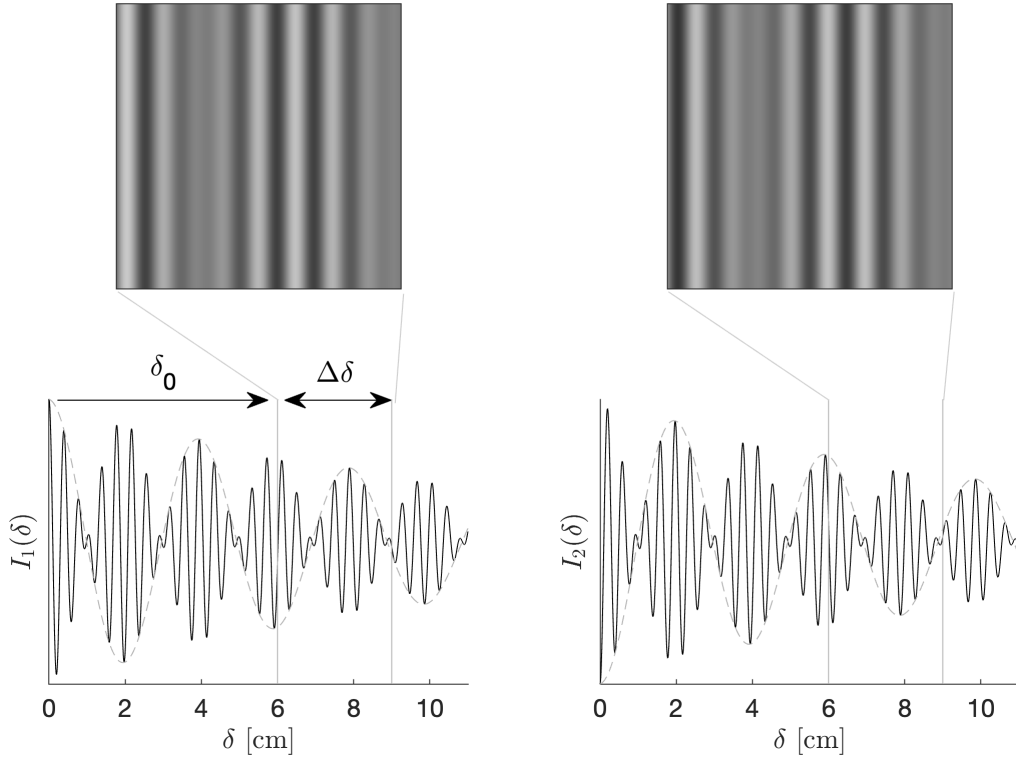
Fig. 3. Noiseless representations of the interferograms imaged
by the two array detectors (top) and cross-sections of those
interferograms (bottom). An OPD (δ) from δ_0 (6 cm) to $\delta_0 +$
$\Delta\delta$ (9 cm) is illuminated in this example. The amplitude of the
Littrow heterodyne envelope decays exponentially with the
OPD according to the Brillouin linewidth and oscillates with a
spatial frequency that depends on the Brillouin shift.

After acquiring the two interferograms, a ratio of the interferograms, what
will be referred to here as the "normalized interferogram," is formed to isolate
the terms that depend only on the Brillouin shift (ν_B), Brillouin linewidth (Γ_B),

11

164 ratio of elastic to inelastic scatter (γ), and Littrow heterodyne frequency ($\nu_L -$

165 ν_0).

$$Q(\delta) = \frac{I_1(\delta) - \left(\frac{\eta_1 a_1}{\eta_2 a_2}\right) I_2(\delta)}{M_2{}'(\delta) I_1(\delta) + M_1{}'(\delta) \left(\frac{\eta_1 a_1}{\eta_2 a_2}\right) I_2(\delta)} \tag{8}$$

$$= \left[\frac{1}{1+\gamma} \exp(-\pi \Gamma_B \delta/c) \cos(2\pi \nu_B \delta/c)\right.$$

$$\left. + \frac{\gamma}{1+\gamma}\right] \cos(2\pi(\nu_L - \nu_0)\delta/c)$$

166 $(\eta_1 a_1)/(\eta_2 a_2)$ is referred to here as the "gain ratio" and can be obtained by

167 taking the ratio of the interferograms averaged over the spatial period of the

168 Littrow heterodyne, or, ideally, by observing a white light source like solar

169 background. $M_1{}'(\delta)$ and $M_2{}'(\delta)$ can be determined using scatter from the water

170 surface, or by episodically injecting a narrowband source. The Littrow

171 heterodyne period can be continually assessed using any available Brillouin or

172 elastic scatter.

173   From Eq. (8), the OPD offset that will maximize the sensitivity of the

174 amplitude and phase of the envelope to both Brillouin linewidth and shift,

175 respectively, is $\delta \cong c/(\pi \Gamma_B)$. For an OPD that falls within the optimum range

176 for water temperatures between 0 and 35 °C and a transmitter with a 10 ns pulse

177 width or greater and transform limited spectral width, the factors $M_1{}'(\delta)$ and

178 $M_2{}'(\delta)$ are vanishingly close to M_1 and M_2, respectively. M_1 and M_2 may still

179 exhibit a dependence on OPD from imperfections, however.

3. Temperature, salinity, and sound velocity error sensitivities

What has been discussed up to this point is the average behavior of the normalized interferogram and its dependence on the Brillouin shift and linewidth. However, the interferograms, once acquired, will have detection noise. The attention now turns to estimating the random errors in the retrievals of Brillouin shift and linewidth caused by detection noise, with further propagation to random uncertainties in temperature, salinity, and sound velocity. The process for determining the variance of the normalized interferogram on account of detection noise on the interferograms, as shown in Appendix A, derives from another work [20] in which the analogous case of a fringe imaged, tilted Mach-Zehnder was studied. A model is fitted to the normalized interferogram to estimate the Brillouin shift, linewidth and elastic scatter ratio parameters, so the Jacobian of the normalized interferogram can be used to obtain the variance and covariance of the parameters, as shown in Appendix B. A second Jacobian describing the sensitivities of the Brillouin shift and linewidth parameters to temperature and salinity can then be used to transform the parameter covariance matrix into a covariance matrix of temperature and salinity, and another transform can be used to convert the covariance matrix of the temperature and salinity to variance in sound velocity, as shown in Appendix C. Only the results are shown in this section.

Estimating uncertainties in temperature, salinity, and sound velocity requires knowing the sensitivities of the Brillouin shift and Brillouin linewidth to

202 temperature and salinity, and the sensitivity of sound velocity to temperature

203 and salinity. Examples of these sensitivities for three water temperatures, a

204 salinity of 35 ppt and 532 nm illumination are provided in Table 1. The sound

205 velocity and its sensitivities derive from [17].

206 **Table 1. Sensitivities of the Brillouin shift and linewidth and sound**

207 **velocity to temperature and salinity.**

		5 °C	15 °C	25 °C
$\partial v_B/\partial T$	MHz/°C	20.2	15.4	11.5
$\partial \Gamma_B/\partial T$		-76.1	-34.0	-13.1
$\partial v_B/\partial S$	MHz/ppt	7.52	6.94	6.49
$\partial \Gamma_B/\partial S$		2.05	1.33	1.02
$\partial V_s/\partial T$	m/s/°C	4.06	3.16	2.41
$\partial V_s/\partial S$	m/s/ppt	1.28	1.17	1.08

208

209 A numerical example is provided to check the accuracy of results from the

210 analytical expressions derived in Appendices A through C against a Monte

211 Carlo scheme. The parameters in Table 2 are assumed for the numerical

212 example and will also be assumed for the lidar simulations later. The

213 uncertainties pertain to a salinity of 35 ppt and 532 nm illumination. Also, the

214 pixel density is assumed to be large compared to the Littrow heterodyne

215 wavenumber (i.e., $P/\Delta\delta \gg |\nu_L - \nu_0|/c$), and the pixels are assumed to be large

216 enough that the covariance (i.e., optical crosstalk) between neighboring pixels

217 can be neglected.

218 **Table 2. Parameters assumed for the calculation of uncertainties.**

γ	0.1
$\|\nu_L - \nu_0\|$	76.1 GHz
$\Delta\delta$	3 cm
δ_0	6 cm
F_B	-1
M_i	0.8

219

220 The Monte Carlo random error estimates are obtained by creating Poisson

221 random realizations of the two interferograms, computing the normalized

222 interferogram, applying a least-squares fit to obtain the Brillouin shift and

223 linewidth, then solving iteratively for temperature and salinity using Eq. (C 1).

224 The process is repeated 1,000 times to obtain statistics. The sound velocity is

225 then computed for each retrieved set of temperature and salinity. The standard

226 deviations of the retrieved temperature, salinity, and sound velocity across

227 iterations are computed and then normalized to SNR [Eq. (A 8)] to derive the

228   inverse sensitivity. Results for a range of temperatures and salinities are shown

229   in Table 3 alongside the corresponding analytical result.

230   **Table 3. Comparisons of estimates of inverse sensitivity in temperature,**

231   **salinity, and sound velocity for the analytical and Monte Carlo methods**

232   **for a range of temperatures and salinities typical of natural water bodies.**

233   **The inverse sensitivities are divided by the SNR to obtain the random**

234   **error in the corresponding quantity.**

		0 °C		15 °C		30 °C	
		0 ppt	35 ppt	0 ppt	35 ppt	0 ppt	35 ppt
ΔT $\cdot SNR$ [°C]	Analytical	108	120	170	183	644	667
	Monte Carlo	110	127	167	200	553	710
ΔS $\cdot SNR$ [ppt]	Analytical	1,207	1,069	587	532	1,042	1,022
	Monte Carlo	1,253	1,125	599	560	935	1,064
ΔV_S $\cdot SNR$ [m/s]	Analytical	1,628	1,582	669	608	606	561
	Monte Carlo	1,632	1,616	697	605	586	585

235

236   The agreement between the analytical and Monte Carlo method results in

237   Table 3 across temperature and salinity provides confidence in the accuracy of

238   the analytical model results. The contour plots in Fig. 4 show the 1σ random

239   error maps for an SNR of unity across OPD range ($\Delta\delta$) and offset (δ_0) for

temperature (ΔT), salinity (ΔS) and sound velocity (ΔV_s) estimated by the
analytical method.
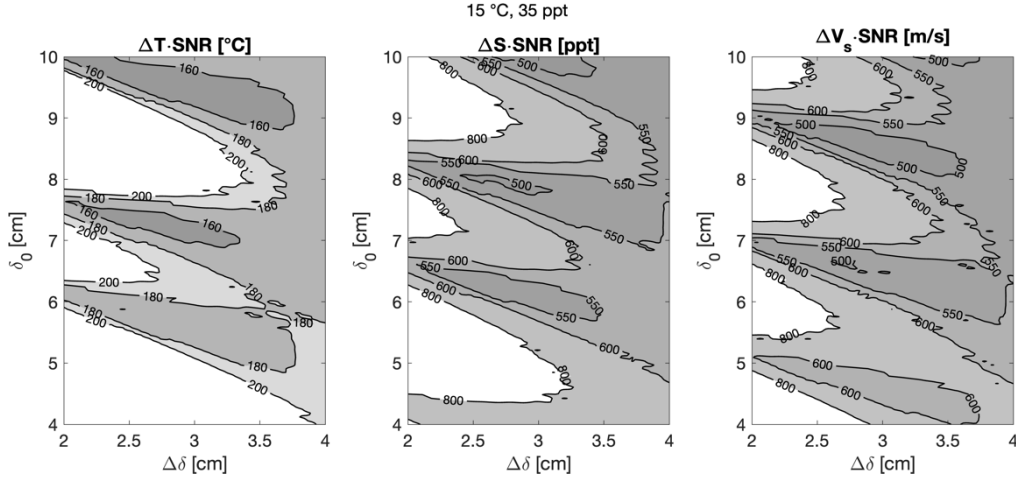
Fig. 4. Contour plots of 1σ random error in temperature, salinity,
and sound velocity (left to right) for an SNR of unity, water
temperature of 15 °C and a salinity of 35 ppt across OPD range
(horizontal axis) and OPD offset (vertical axis).

Fig. 4 can be used to select an optimum OPD range and OPD offset for the
target application. Once an OPD offset and range are selected, the sensitivities
to temperature, salinity, and sound velocity can be derived using the process
outlined above and combined with SNR from lidar simulations to estimate the
random errors for each quantity. The sections that follow are dedicated to
deriving this SNR.

To compare the sensitivities of Brillouin spectrometers, it is sometimes
instructive to express the Brillouin shift random error in terms of a multiple (α)

255 of the Brillouin linewidth divided by the SNR (i.e., $\Delta v_B = \alpha \Gamma_B / SNR$), as some

256 authors, e.g. [2,7], have done. A BASH with an OPD offset of 6 cm and an OPD

257 range of 3 cm and no defects achieves an α of between 3.1-3.3 from 5 °C to 25

258 °C when elastic scatter is negligible compared to Brillouin scatter.

259 **4. Discussion on operating altitude, field of view and collection area**

260 After determining OPD range and OPD offset, the next design choice is the

261 operating altitude and telescope size. It is desirable to have a receiver footprint

262 size of at least 6 m on the ocean surface for near-coastal water types [21]. A

263 footprint of this size will allow efficient collection of multiple scatter from

264 depth, making the apparent attenuation of the beam with depth closer to what's

265 referred to as the *diffuse attenuation coefficient*. Receivers with narrower fields

266 of view and limited multiple scatter collection result in attenuation that is closer

267 to the *beam attenuation coefficient*, which is much higher than the diffuse

268 attenuation coefficient, and even more so for productive, coastal water types.

269 For example, for waters with a chlorophyll concentration of 1 mg/m^3, the

270 diffuse attenuation is about 0.1 /m whereas the beam attenuation is 0.25-0.4 /m.

271 Therefore, an apparent attenuation closer to beam attenuation would, for the

272 same SNR, provide 2.5-4 times less penetration. For a field of view that

273 provides a 6 m receiver footprint on the ground, the amount of scatter collected

274 will scale directly with the acceptance etendue ($A\Omega$) of the receiver, so it is

275 desirable for an ocean lidar receiver to accommodate a large etendue.

276　　　A larger field of view will also allow diverging the transmit beam such that

277　　　the energy density at the surface is below levels that would be harmful to

278　　　humans or marine life. A 2 m dia. ($1/e^2$) Gaussian beam with a 2 mJ energy has

279　　　a peak energy density of $1.3 \cdot 10^{-7}$ J/cm^2, which is below the maximum

280　　　permissible exposure (MPE) for a 10 ns, 532 nm laser pulse. At a pulse

281　　　repetition rate of 4 kHz, the average power density is $5.2 \cdot 10^{-4}$ W/cm^2, which is

282　　　below the MPE for all exposure durations. A large etendue therefore also has

283　　　advantages for eye safety.

284　　　For most receivers, the etendue of the highest spectral resolution optic will

285　　　govern the etendue of the receiver. The Brillouin spectrometer will likely be the

286　　　highest spectral resolution optic in this application. An advantage of

287　　　spectrometers employing the BASH technique is that they can be (and often

288　　　are) field widened. Field widening is achieved by introducing refractive

289　　　elements in the arms of the interferometer to create a 'quasi-zero' path

290　　　difference condition in which the rays from each arm emerge mostly parallel

291　　　and coincident with each other while still having experienced a non-zero optical

292　　　path difference. This has the effect of enhancing the field of view and etendue

293　　　of the interferometer. In the case of the BASH, field widening is accomplished

294　　　by inserting a prism in each arm. The case of prisms with an index of refraction

295　　　greater than two will be assumed here. The ray tracing algebra was worked out

296　　　in [22] for this case, which finds the quartic angular dependence of the OPD

297　　　shown in Eq. (9).

$$\delta(\vartheta) \approx \delta(0) + \frac{\delta(0)}{16n^2}\vartheta^4 \tag{9}$$

298      $\delta(0)$ is the OPD for a ray at normal incidence, ϑ is the off-axis angle and n

299   is the index of refraction of the prisms. The impact to the visibility factors M_1

300   and M_2 can be assessed by integrating the cosine of the phase deviation caused

301   by the OPD deviation $\delta(\vartheta) - \delta_0$ over the distribution of ray angles $f(\theta)$, i.e.

$$M_\Omega = \int_\Omega f(\vartheta) \cos\big(2\pi\big(\delta(\vartheta) - \delta(0)\big)/\lambda\big) \, d\Omega \tag{10}$$

302   Assume a uniform, circular distribution of ray angles that extend up to a half

303   angle of θ_M. The etendue-limited visibility factor is then, after series expansion

$$M_\Omega \approx 1 - \frac{\pi^2}{640n^4}\left(\frac{\delta_0}{\lambda}\right)^2 \theta_M{}^8 \tag{11}$$

304   M_1 and M_2 are both degraded by the factor M_Ω, but note the 8th order

305   dependence on divergence. For water-clear ZnS prisms with an index of

306   refraction of 2.40 at 532 nm and an OPD offset of 9 cm, >99.9% of the visibility

307   can be preserved by limiting the incident ray angle divergence to a half angle

308   of 50 mrad. If the interferometer's aperture is 2.5 cm × 2.5 cm, the aircraft's

309   altitude is 300 m, and the receiver's full angle field of view is 6 m/300 m ~ 20

310   mrad, the telescope's collection area can be as large as 12.5 cm × 12.5 cm (156

311   cm^2) while still satisfying the above angular limits. A 156 cm^2 collection area

312   and 300 m flying altitude will be assumed in the simulations later in this work.

313   It should be noted that the ZEMAX ray trace model for this same case [22]

314 showed higher angular sensitivity than that predicted by Eq. (9), which used

315 small angle approximations. A more detailed study with ray tracing software is

316 warranted.

317 To illustrate the value of field widening for this application, consider a

318 comparison with the Fabry-Perot interferometer (FPI) and virtually imaged

319 phased array (VIPA) that have previously been studied for use in Brillouin

320 spectroscopy [23-27]. For a shift of half a fringe across the solid angle of

321 acceptance, the limiting etendues [22] for receivers employing an FPI/VIPA

322 and BASH are

$$(A\Omega)_{FPI/VIPA} = A\frac{2\pi}{R} \qquad (12)$$

$$(A\Omega)_{BASH} = A\frac{2\sqrt{2}\pi}{\sqrt{R}}n \qquad (13)$$

323 Where R is the interferometer's resolving power and A is the area of its

324 useable aperture. The resolving power for the BASH specified in Section 3 is

325 $\delta/\lambda \sim 10^5$. The limiting etendue for an FPI with the same aperture and

326 resolving power, by Eqs. (12) and (13), would be approximately 1,000 times

327 less than that of the BASH. An FPI and VIPA with equal resolving power will

328 have a similar solid angle of acceptance, but the VIPA has the additional

329 constraint of requiring that the input light pass through a narrow effective

330 entrance slit to get past the edge of a high reflection coating, greatly limiting its

331 useable aperture [28]. The BASH therefore collects at least 1,000 times more

332   scatter and will achieve at least $\sqrt{1000} \approx 32$ times higher SNR than an FPI or

333   VIPA for this wide field of view, eye safe lidar. Accurate measurements of the

334   Brillouin shift or linewidth by the FPI or VIPA may also be confounded by

335   changes in the diffuseness of the scatter with depth.

336   **5.   Random errors in temperature, salinity, and sound velocity**

337   The parameters in Table 4 will be assumed for the lidar simulations. The aircraft

338   will be assumed to fly at an altitude of 300 m and at a speed of 130 m/s (250

339   kts). The laser transmitter parameters are borrowed from NASA Langley

340   Research Center's HSRL-1 airborne high spectral resolution lidar [29]. The

341   photon detection efficiency and excess noise factor figures are consistent with

342   commercial intensified cameras with a filmless MCP, GaAsP photocathode and

343   fast (ns) gating function. A thin film interference filter suppresses solar

344   background, limiting the effective passband to 0.5 nm. A polarizing element

345   directs the depolarized component of the backscatter to another detector. Since

346   the Brillouin backscatter is mostly copolarized with the transmitter and the solar

347   background is mostly depolarized, the polarizer affords a further factor of ~two

348   reduction in solar background while efficiently transmitting the Brillouin

349   scatter. It should be noted that, by Eqs. (B 3) and (B 4), the sensitivity to

350   Brillouin shift and linewidth will decrease when elastic scatter is present, and

351   elastic scatter may be ~10 times stronger than Brillouin scatter for more

352   productive waters. To mitigate the impact of elastic scatter on the sensitivity,

353 the backscatter will transmit through an iodine cell before the BASH and the

354 laser transmitter will be tuned to an absorption feature of iodine that suppresses

355 elastic scatter and efficiently passes the Brillouin scatter, as is done in HSRL-1

356 to implement the high spectral resolution lidar technique [29]. A functionally

357 similar alternative to the iodine cell would be a field widened Michelson with

358 a free spectral range of twice the Brillouin shift [30], and this approach would

359 not be limited to wavelengths that correspond to absorption lines.

360 **Table 4. Lidar instrument parameters assumed for the simulations.**

E_p	Energy per pulse	2 mJ
PRF	Pulse repetition frequency	4 kHz
λ	Wavelength	532 nm
η_t	Transmit optics efficiency	90%
η_r	Receiver optics efficiency	50%
A	Receiver collection area	156 cm^2
FOV	Receiver field of view, full angle	20 mrad
L	Lidar altitude	300 m
$\Delta\lambda$	Receiver effective passband	0.5 nm
η	Photon detection efficiency	50%
F	Excess noise factor, power space	2.6

361

362   The geophysical variables in Table 5 will be assumed for these simulations.

363   The apparent attenuation is assumed to be constant with depth and equal to the

364   diffuse attenuation coefficient. The depolarization ratio is also assumed to be

365   constant with depth.

366   **Table 5. Geophysical parameters assumed for the simulations. Mm is**

367   **megameter (10^6 m).**

T_a	One-way atmospheric transmittance	95%
T_s	One-way surface transmittance	98%
K_d	Diffuse attenuation coefficient	0.1 /m
β_{sw}	Seawater backscatter coefficient	232 /Mm/sr
δ_{sw}	Seawater depolarization ratio	0.039
n_{sw}	Seawater index of refraction	1.34
$L_{e,\Omega,\lambda}$	Upwelling solar radiance	7.5 mW/m^2/sr/nm

368

369   The following equations describe the number of Brillouin backscatter (N_A)

370   and solar background (N_B) photons received from a range bin with a vertical

371   extent (depth resolution) of Δz at a depth of z after integrating M laser shots.

372   Backscatter (and background) photons from M laser pulses are accumulated in

373   a single exposure of (e.g.) a CCD or CMOS frame by triggering the intensified

374 cameras' gate M times before finishing the exposure and reading the frame.

375 There would be one exposure for each depth.

$$N_A$$

$$= M \frac{E_p}{hc/\lambda} \eta_t \eta_r T_a{}^2 T_s{}^2 \exp(-2K_d z) \beta_{sw} \frac{1}{\delta_{sw}+1} \frac{A}{(n_{sw}L+z)^2} \Delta z \tag{14}$$

$$N_B = M \frac{1}{2} \frac{L_{e,\Omega,\lambda}}{hc/\lambda} \eta_r \pi \left(FOV \frac{L}{2}\right)^2 \frac{A}{L^2} \frac{2\Delta z}{c/n_{sw}} \tag{15}$$

376 The delay of the intensified camera gate relative to the emission of the laser

377 pulse is varied to sequentially probe each range bin. The gate width will be

378 assumed to be fixed at 9 ns, which will provide a depth resolution of 1 m. Gate

379 widths of <2 ns are possible with some cameras. The number of laser shots

380 accumulated at a particular depth will vary exponentially with depth such that

381 the SNR is mostly constant, with exponentially more shots required at greater

382 depths. By this scheme, the overall time it takes for a gated, intensified camera

383 with a maximum frame rate R_F to acquire N interferograms throughout a profile

384 covering 0 to z_0 depth, with the number of shots increasing exponentially with

385 depth according to the expected diffuse attenuation ($K_d{}'$) until reaching a

386 maximum of t_0 at the deepest point z_0, will then be

$$\frac{N}{R_F} + t_0 \sum_{i=1}^{N} \exp(-2K_d{}' z_0 (i-1)/N)$$

$$= \frac{N}{R_F} + t_0 \frac{1 - \exp(-2K_d{}' z_0)}{1 - \exp(-2K_d{}' z_0/N)} \tag{16}$$

387   Assume 1 s (4,000 shots) of accumulation at the deepest point and a camera

388   frame rate of 15 Hz. The time it takes to acquire a profile of 1 m resolution

389   through a column extending to 30 m depth is then 7.5 s, over which time the

390   aircraft, flying at 130 m/s, has traversed 975 m horizontally. For a K_d' of 0.3

391   /m and the same depth resolution (1 m), a profile extending 3 optical depths

392   takes 2.9 s to acquire while the aircraft traverses 374 m horizontally. Table 6

393   shows the expected number of backscattered and solar background photons, the

394   SNR in day and night, and the corresponding uncertainties in temperature,

395   salinity, and sound velocity at 30 m depth with 1 m resolution. The SNR and

396   background parameters come from Eq. (A 8) and Eq. (A 9), respectively. The

397   sensitivity is based on a temperature of 15 °C and salinity of 35 ppt. The

398   variance contributed by the dark noise and readout noise of the intensified

399   camera is assumed to be negligible compared to that contributed by shot noise

400   from backscatter.

401   **Table 6. Cumulative backscatter and background photon number,**

402   **corresponding SNR, background parameter, and temperature, salinity,**

403   **and sound velocity 1σ random error for day (left column) and night**

404   **(right column) operation. These correspond to a 1 m bin at 30 m depth**

405   **with 1 second of averaging (4,000 shots) in water with a diffuse**

406   **attenuation of 0.1 /m.**

	Daytime	Nighttime
N_A	385,000	
N_B	441,000	0
SNR	186	272
F_B	0.07	-1
ΔT (1-σ)	1.05 °C	0.67 °C
ΔS (1-σ)	2.97 ppt	1.95 ppt
ΔV_S (1-σ)	3.36 m/s	2.23 m/s

407

408 For the 3 cm OPD range and 6 cm OPD offset specified for this design, the

409 random errors in temperature are larger than those shown in Table 6 for warmer

410 waters. However, dense cooler waters will typically exist below warmer waters

411 and so cooler waters shall, in general, be more SNR starved than warmer waters

412 and therefore demand a higher sensitivity if measurement of temperature is the

413 objective. Conversely, for sound velocity, the warmer waters produce lower

414 uncertainties for this design. Other choices of OPD range and offset may

415 therefore be more optimal, depending on the target application. Fig. 5 shows a

416 profile of daytime retrievals of temperature, salinity, and sound velocity and

417 associated 1σ random errors for a temperature/salinity profile that is 25 °C/32

418 ppt from 0-10 m depth, descends linearly to 10 °C/34 ppt between 10-15 m

419 depth, and remains at that level from 15-30 m depth. The diffuse attenuation

420 coefficient is 0.1 /m throughout, so an optical depth of three corresponds to 30

421 m. This profile is meant to be representative of a sounding through a cold pool

422 [31].

423
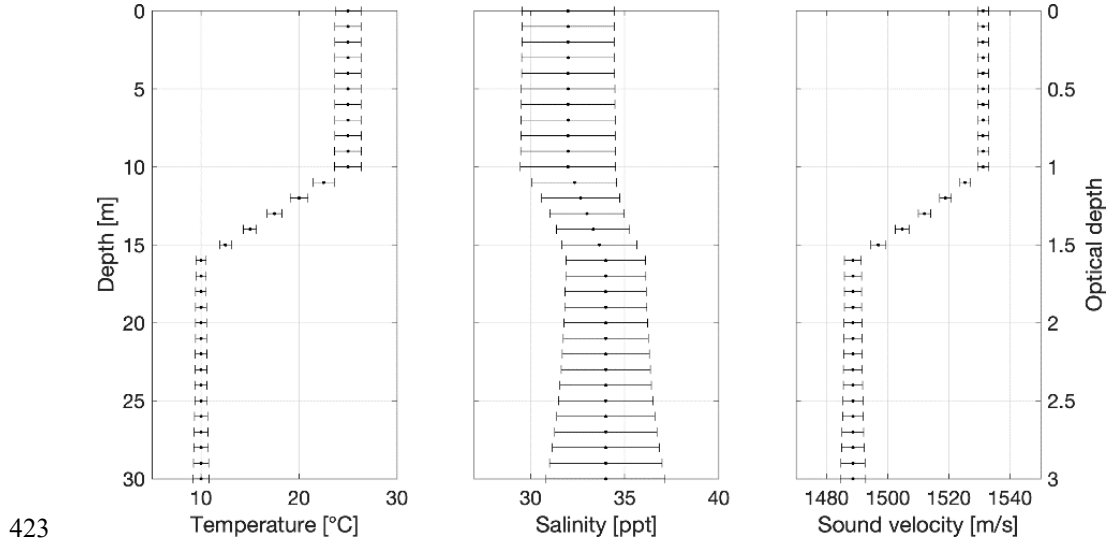
424 Fig. 5. Retrieved temperature, salinity, and sound velocity with

425 error bars showing 1σ random errors for optical depths of up to

426 three during daytime. The physical depth resolution is 1 m and

427 horizontal resolution is 1 km for this 0-30 m profile.

428 Using the camera gating scheme outlined above, the SNR is approximately

429 constant throughout the column. The larger uncertainties in temperature and

430 salinity at shallower depths in Fig. 5 are therefore due to the lower sensitivities

431 to those quantities at higher temperatures. Fig. 5 shows that the gradient in

432 temperature and sound velocity would be easily resolved, but not the salinity

433 gradient.

434   For some applications, less depth penetration in exchange for finer

435   horizontal resolution is preferable. For example, salinity profiles extending just

436   one optical depth (or less) would be useful for mapping freshwater lenses and

437   outflows. Temperature profiles extending two optical depths would be

438   sufficient for profiling the active mixing layer across most of the ocean and

439   determining the intensity, location and size of eddies and ocean fronts. These

440   applications require a horizontal resolution sufficient to capture submesoscale

441   feature lengths (~100's m). With these objectives in mind, Fig. 6 shows the

442   daytime random errors in temperature, salinity, and sound velocity across

443   horizontal resolution and maximum profile depth. A fixed temperature/salinity

444   of 15 °C/35 ppt is assumed, along with a depth resolution of 1 m and 0.1 /m

445   apparent attenuation.
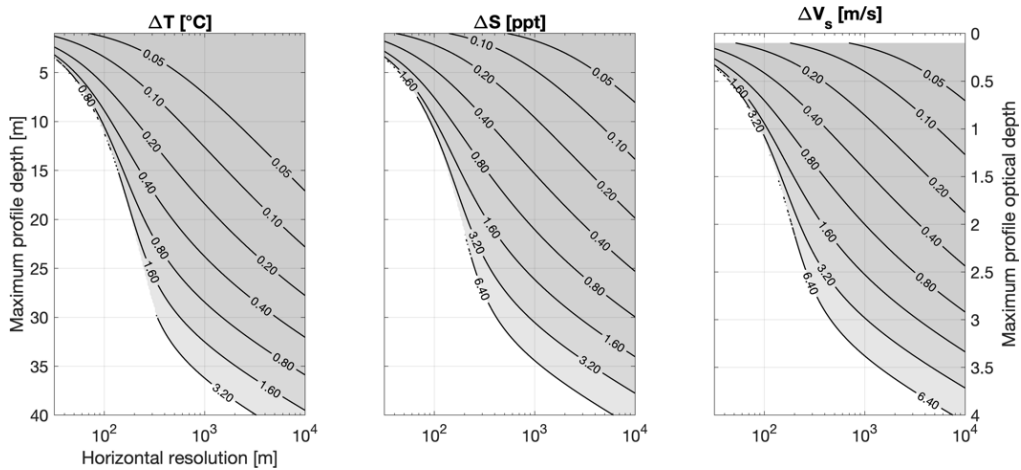
446

447   Fig. 6. A mapping of daytime random errors in temperature,

448   salinity, and sound velocity for different horizontal averaging

449   scales and maximum profile depths (i.e., deepest extent of the

| 450 | profile). Contours are truncated where the number of shots at |
| 451 | the surface would be <1. |

6. Systematic errors in temperature, salinity, and sound velocity

Major sources of systematic error will be knowledge of the visibility factors, knowledge of the Littrow heterodyne period, knowledge of solar background, knowledge of gain ratio, knowledge of the linearity of the intensified camera, and any variations in the spectral transmittance of the elastic scatter suppression filter that might alter the apparent, relative strengths of the two Brillouin doublet peaks ("Brillouin doublet imbalance"). The sensitivities of the measurements of temperature, salinity, and sound velocity to each of these factors are now investigated. This is done by performing a retrieval against a "truth" temperature, salinity, and sound velocity and then introducing small perturbations in the retrieval parameters to observe their effect on the retrieval, which is essentially the same process as the Monte Carlo method outlined earlier but with the random errors from detection noise replaced with systematic errors in the retrieval inputs. The temperature is 15 °C, salinity is 35 ppt, solar background is equal to backscatter ($F_B = 0$), gain ratio is assumed to be unity, and the two visibility factors are assumed to be 0.8. The sensitivities are shown in Table 7.

Table 7. First order propagation of systematic errors in visibility factors, Littrow heterodyne phase, solar background, gain ratio and Brillouin

471   **doublet imbalance to errors in temperature, salinity, and sound velocity.**

472   **Values are the errors in T, S, or V_s per percent or radian error in the**

473   **parameter indicated in left column.**

	ΔT (°C)	ΔS (ppt)	ΔV_s (m/s)
Visibility factor	-0.34 /%	0.74 /%	-0.21 /%
Littrow heterodyne phase	0.81 /rad	-1.03 /rad	1.35 /rad
Solar background	0.37 /%	-0.78 /%	0.25 /%
Gain ratio	-0.049 /%	-0.048 /%	-0.21 /%
Intensified camera linearity	0.016 /%	-0.030 /%	0.015 /%
Brillouin doublet imbalance	0.002 /%	0.005 /%	0.011 /%

474

475   For retrievals at the shallowest depths (<5 m), or during nighttime, the solar

476   background error sensitivity becomes negligible, but the linearity error

477   sensitivity amplifies to -0.21 °C/% in temperature, 0.46 ppt/% in salinity and -

478   0.12 m/s/% in sound velocity and becomes the dominant error source. Both the

479   Littrow heterodyne phase and gain ratio can be assessed frequently and are

480   expected to be stable on profile acquisition timescales (~10 s). A phase error on

481   the order of a few mrad and gain ratio error of 1% is probably achievable,

482   making these error contributions to temperature and salinity negligible. The

483   gain ratio error is still significant to the sound velocity, however. The linearity

484 error could be made small by characterizing the camera's response. By Table

485 7, the sensitivity to error from Brillouin doublet imbalance is very small.

486 Therefore, the major sources of error in temperature and salinity are likely to

487 be the knowledge of the visibility factors and, for daytime operation and

488 retrievals from depth, knowledge of the solar background. The solar

489 background would need to be measured continually on a separate detector that

490 is episodically cross calibrated with the intensified camera. If we assume 1%

491 errors in the visibility factors, solar background and gain ratio, the root sum of

492 square errors in temperature, salinity, and sound velocity are 0.5 °C, 1.1 ppt,

493 and 0.4 m/s, respectively. Accurate knowledge of the visibility factors and solar

494 background will be more critical for warmer waters because the temperature

495 sensitivity of the Brillouin linewidth is significantly lower at warmer

496 temperatures. At 25 °C, the sensitivity to visibility factor error ~doubles to

497 about -0.8 °C/%, 1.5 ppt/% and -0.4 m/s/% and the sensitivity to solar

498 background error also ~doubles to 0.9 °C/%, -1.6 ppt/% and 0.5 m/s/% with

499 respect to the 15 °C case. A version of the retrieval of temperature that uses

500 only the Brillouin shift parameter – with assumption about salinity and errors

501 associated with that assumption – might therefore be more accurate for warmer

502 waters. An error of about 0.4 °C/ppt can be expected under this assumption

503 [32]. Substantially smaller errors in gradient measurements can be expected.

504 Also, absolute errors will be smaller if measurements can be periodically

505 "pinned" to coincident, collocated measurements from *in-situ*, microwave/IR

derived sea surface temperature (SST), microwave derived sea surface salinity

(SSS), or other sources.

Another potential source of systematic error is the effect of multiple scatter

on the backscatter spectrum. Simulations [33] have shown minimal corruption

of the Brillouin backscatter spectrum by multiple scatter, reasoning that since

particulates predominantly forward scatter that a direct backscatter by the

Brillouin process was significantly more probable than scatter at any other

angle for productive waters. For a purely Brillouin scattering water body more

corruption was noted, but this scattering regime is not seen in natural water

bodies, even in the open ocean. The effect of multiple scatter could be modeled

and quantified, but efforts to accurately model multiple scatter are often

confounded by inaccurate knowledge of the particulate scatter phase

function(s) for a particular water body. Other potential sources of error could

be inexact knowledge of the bulk and shear viscosities as a function of

temperature and salinity, so these might need to be verified in a water tank

demonstration, or the measurements episodically pinned to other temperature

and salinity data sources.

7. Conclusions and science outlook

An airborne Brillouin lidar capable of scientifically and operationally

meaningful remote sensing measurements of temperature, salinity, and sound

velocity is practical with current technology. The concept presented here

527   achieves an expected daytime (nighttime) random error of 1.1 °C (0.7 °C) in

528   temperature, 3.0 ppt (2.0 ppt) in salinity, and 3.4 m/s (2.2 m/s) in sound velocity

529   throughout a column that extends three optical depths with a depth resolution

530   of 1 m and horizontal resolution of 1 km. Similar performance is obtained for

531   profiles extending two (one) optical depths with a horizontal resolution of 200

532   m (100 m). The main sources of systematic error are the errors in knowledge of

533   the visibility factors and solar background, which might need to be known to

534   the sub-percent level for warmer waters, depending on requirements. Error in

535   the knowledge of the visibility factor, like other errors, would depend on the

536   accuracy with which the visibility factors can be assessed, combined with the

537   rate of these assessments and the rate of change between assessments. This and

538   the camera characterization would need to be part of a future study. More

539   advanced laser and detector technologies on the horizon could significantly

540   enhance performance beyond that shown here. A laser transmitter that emits in

541   the blue (470-490 nm) would offer twice the penetration depth in less

542   productive waters typical of the open ocean. Projects focused on the

543   development of blue laser transmitter technology are currently active in the US

544   and elsewhere. A large array of single photon sensitive elements (e.g., single

545   photon avalanche diodes) with integrated electronics that allow timing all

546   photons received from throughout the column would improve the horizontal

547   resolution of profiles extending three optical depths from 1 km to ~100 m and

548 the lower excess noise factor could afford a factor of ~1.6 reduction in random

549 error relative to existing intensified cameras. Such arrays are also being studied.

550 The Brillouin lidar receiver described herein would require a single mode

551 laser transmitter that is frequency stable and perhaps also frequency agile to a

552 limited degree. Workhorse airborne lidars with such transmitters and receivers

553 of similar size and complexity are deployed routinely by NASA [11-14, 29], so

554 a Brillouin lidar system based on this BASH spectrometer receiver concept

555 would be compact and lightweight enough to fly economically on one of

556 NASA's smaller aircraft, e.g., de Havilland Canada DHC-6 Twin Otter,

557 Beechcraft B200 King Air, or suitable unpiloted aerial vehicle (UAS) for near

558 shore operations as well as large aircraft for distant or longer duration

559 operations. The depth to which measurements can be made is limited to a few

560 10's of meters, paling in comparison to the depths possible with moorings,

561 floats, and ship-based sensors. However, an airborne sensor has unique

562 advantages in terms of deployment flexibility and spatial coverage. Such a lidar

563 could be quickly targeted to remote domains of specific interest by flying in a

564 fuel-efficient mode at cruise altitude and then acquiring low altitude

565 measurements over hundreds to thousands of kilometers at a sampling density

566 of the order 1 /km or better, providing synoptic scale transects containing

567 hundreds to thousands of profiles of temperature and salinity in a matter of

568 hours and at much lower cost than soundings from a ship or airborne

569 expendable bathythermographs and conductivity-temperature-depth (CTD)

probes. Such a lidar could complement *in-situ* sensors by improving their targeting and providing a means for cross calibration. A lidar sensor would also not suffer the thermal lag problem experienced with CTD sensors due to the thermal mass of the sensor. The absence of thermal lag errors would have significant advantages in resolving the depth of layers that have a steep gradient in temperature, like cold pools [34, 35].

There are many potential science applications for an airborne Brillouin lidar. Profiles from a lidar based on the BASH technique would provide valuable information on mixed layer depth and the location, size, and intensity of eddies, ocean fronts, cold pools, freshwater lenses, and freshwater outflows, and could be used to study the fate of meltwater from sea ice and glaciers at high latitudes, and its influence on upper ocean stratification and phytoplankton blooms [36]. Moreover, it would be straightforward to add simultaneous measurement of particulate backscatter, which can be used to estimate phytoplankton biomass and investigate phenomenon like diel vertical migration of zooplankton and other marine animals. There are many potential science applications for an airborne Brillouin lidar.

As a specific application, consider measurements of the position of the Mid-Atlantic Bight (MAB) Cold Pool, which is spatiotemporally variable [37] and is of prime importance for understanding the path and evolution of approaching storms, especially tropical cyclones [38], and for predicting the movement of fish species [39]. Mixing by tropical cyclones of the abundant cold bottom

water in the MAB with warmer surface water is known to be capable of causing

rapid deintensification, as in the case of Hurricane Irene (2011) prior to its New

Jersey landfall as an example [40]. In contrast, Hurricane Sandy (2012) was

able to cause immense destruction across New Jersey and New York because

of the disappearance of the Cold Pool off the coast that season [41], which

usually serves as a barrier to such storms. Model assimilation of rapidly

acquired temperature profiles across tropical cyclone tracks could therefore

improve forecasts and prevent excessively early or unnecessary evacuations.

For major population centers, reducing decision lead times from 72 to 48 hours

could save hundreds of millions of dollars in evacuation costs annually [42].

The MAB Cold Pool is warming and shrinking [43], speaking to the need for

more observations to track its evolution. There is also interest in understanding

the impact of offshore wind farm pylons on stratification of the MAB Cold Pool

[44], and implications for storms and fisheries. A temperature profiling lidar

could perform raster maneuvers around offshore wind farms to address this

observational need. Assimilation of lidar measured temperature profiles could

improve the skill of circulation models developed for the MAB and Gulf of

Maine that currently only assimilate data from satellite SST and *in-situ* sources

[45]. Root-mean-square errors of 0.86-4.64 °C were observed between

Saildrone and SST data [46], with the greater errors near the coast in summer

where (and when) reliable temperature data is most critical for storm

forecasting, compared with errors of 0.5 °C for the BASH. The value of the

614 BASH technique for forecasts of hurricane trajectory and intensification to the

615 open ocean. Hurricane trajectory models would benefit from assimilation of

616 temperature and salinity profiles from lidars installed on long-range, long-

617 duration Hurricane Hunter aircraft, e.g., NOAA's Lockheed WP-3D Orion fleet

618 and the Air Force Reserve's Lockheed-Martin WC-130J fleet, to fill gaps

619 between bathythermographs and CTD probes.

620 Another application of data from such a lidar would be improvement to

621 forecast models for red tide algal bloom events, e.g., off the West Florida

622 Continental Shelf [47]. Such blooms can evolve rapidly, and forecasts would

623 benefit from assimilation of temperature and salinity observations from an

624 airborne lidar to sensitive regions, and to improve targeting of *in-situ* assets.

625 General benefits of this temperature/salinity technique for many applications

626 include the ability for rapid targeted deployment and the ability to make

627 observations below clouds that thwart satellite SST retrievals. This lidar, if

628 developed, could have significant societal benefits for the US Atlantic and Gulf

629 Coast regions, and perhaps other regions with similar climates, e.g., the Indian

630 Ocean and Pacific Ocean typhoon basins.

631 Most of the applications above relate to temperature measurement, but there

632 is also significant interest in near-surface measurements of salinity. Microwave

633 (L-band) SSS instruments struggle to resolve submesoscale feature lengths,

634 even from aircraft. Also, in contrast with the Brillouin techniques, L-band SSS

635 retrievals are more challenged in cooler Arctic or near polar waters. A Brillouin

636   lidar could provide unprecedented horizontal resolution of near-surface salinity

637   in these regions. Such measurements would therefore be well suited to studying

638   inflows into the ocean from ice shelf melting that existing remote sensing

639   instruments do not resolve well. A Brillouin lidar could also be well suited to

640   studying freshwater lenses, which are shallow layers of freshwater above

641   saltwater where gradients from 1 ppt to 25 ppt are often seen, and these layers

642   exert strong control over refreezing. River outflows and plumes could be

643   mapped to much higher spatiotemporal resolution than is possible with

644   satellites, which only achieve resolutions of 0.25° (~30 km) in a 2-week period.

645   Reasonable info exists on large rivers like the Amazon, but scant information

646   exists on small rivers that are challenging to observe from space. Brillouin

647   lidars could inform coastal hydrology and the fate of freshwater in river plumes,

648   measure freshwater inputs from rainfall associated with strong convective

649   storms in the inter-tropical convergence zone (ITCZ) and examine freshwater

650   inputs at the ocean surface and the impacts of air-sea fluxes, i.e., heat fluxes. A

651   Brillouin lidar could therefore help provide valuable insight into the climate

652   and societal impacts of the exchange of freshwater and heat with the ocean.

653   **Appendix A: Variance of the normalized interferogram**

654   For simplification, assume that coefficients a_1 and a_2 are unity, that the

655   visibility factors are equal ($M_1 = M_2 = M_i$) and that the detection efficiencies

656   are also equal ($\eta_1 = \eta_2 = \eta$). Consider a two-dimensional image of the

normalized interferogram that is summed along the isophase lines of the Littrow heterodyne fringes (row-wise in Fig. 3) and in which i indexes through each of these P summations.

$$Q'_i = \frac{I_{1,i} - I_{2,i}}{I_{1,i} + I_{2,i}} = M_i Q_i \tag{A 1}$$

Q'_i is the normalized interferogram before correcting for the visibility factor and Q_i is consistent with its definition in Eq. (8). $I_{1,i}$ and $I_{2,i}$ are shorthand for $I_1(\delta_i)$ and $I_2(\delta_i)$, respectively, with

$$\delta_i = \Delta\delta \frac{(i-1)}{P} + \delta_0, \quad i = 1 \dots P \tag{A 2}$$

The variance of the ratio at each index i is approximately

$$\frac{\mathrm{var}\, Q'_i}{\overline{Q'_i}^2} = \frac{\mathrm{var}(I_{1,i} - I_{2,i})}{\left(\overline{I_{1,i}} - \overline{I_{2,i}}\right)^2} + \frac{\mathrm{var}(I_{1,i} + I_{2,i})}{\left(\overline{I_{1,i}} + \overline{I_{2,i}}\right)^2}$$
$$- 2\frac{\mathrm{cov}(I_{1,i} - I_{2,i}, I_{1,i} + I_{2,i})}{\left(\overline{I_{1,i}} - \overline{I_{2,i}}\right)\left(\overline{I_{1,i}} + \overline{I_{2,i}}\right)} \tag{A 3}$$

Where 'var' indicates variance and 'cov' indicates covariance. If the noises on $I_{1,i}$ and $I_{2,i}$ are uncorrelated detection noises, we have

$$\mathrm{var}(I_{1,i} - I_{2,i}) = \mathrm{var}(I_{1,i} + I_{2,i}) = \mathrm{var}\, I_{1,i} + \mathrm{var}\, I_{2,i} \tag{A 4}$$

$$\mathrm{cov}(I_{1,i} - I_{2,i}, I_{1,i} + I_{2,i}) = \mathrm{var}\, I_{1,i} - \mathrm{var}\, I_{2,i} \tag{A 5}$$

The variance of the ratio is then

$$\text{var } Q_i' = \left(1 + \overline{Q_i'}^2\right) \frac{\text{var } I_{1,i} + \text{var } I_{2,i}}{\left(\overline{I_{1,i}} + \overline{I_{2,i}}\right)^2} - 2\overline{Q_i'} \frac{\text{var } I_{1,i} - \text{var } I_{2,i}}{\left(\overline{I_{1,i}} + \overline{I_{2,i}}\right)^2} \qquad \text{(A 6)}$$

667 Define $\overline{N_{A,i}}$ and $\overline{N_{B,i}}$ as the mean number of total backscatter and background

668 photons, respectively, accumulated at index i. If it is assumed that the detection

669 of the signal plus background is shot noise and excess noise limited, then var

670 $I_{1,i} + \text{var } I_{2,i} = \eta F(\overline{N_{A,i}} + \overline{N_{B,i}})$ and $\text{var } I_{1,i} - \text{var } I_{2,i} = \eta F \overline{Q_i'} \cdot \overline{N_{A,i}}$, with F

671 being the excess noise factor of the intensified camera expressed in power

672 (variance) space. The substitutions $\overline{Q_i'} \rightarrow M_i \overline{Q_i}$ and $\text{var } Q_i' \rightarrow M_i^2 \text{var } Q_i$ are now

673 made. The variance of Q_i in terms of its expected value $(\overline{Q_i})$ is then given by

674 Eq. (A 7).

$$\text{var } Q_i = \frac{1 + F_{B,i} M_i^2 \overline{Q_i}^2}{M_i^2 SNR_i^2} \qquad \text{(A 7)}$$

675 Where SNR_i represents the signal-to-noise ratio of the sum of the signal in

676 corresponding pixels of each interferogram at index i

$$SNR_i = \frac{\sqrt{\eta N_{A,i}}}{\sqrt{F(1 + N_{B,i}/N_{A,i})}} \qquad \text{(A 8)}$$

677 And $F_{B,i}$ is defined as the "background factor"

$$F_{B,i} = \frac{N_{B,i} - N_{A,i}}{N_{B,i} + N_{A,i}} \qquad \text{(A 9)}$$

678 The background factor varies between -1 and $+1$, depending on the

679 background relative to the backscatter in that pixel. If both the backscatter and

680 background are uniformly distributed among P pixels, then $SNR_i^2 = SNR^2/P$

681 and $F_{B,i} = F_B$ and the variance of the normalized interferogram at each pixel

682 becomes.

$$\text{var } Q_i = \frac{1 + F_B M_i{}^2 \bar{Q}_\iota{}^2}{M_i{}^2 SNR^2/P} \tag{A 10}$$

683 **Appendix B: Propagation to variance and covariance in Brillouin**

684 **shift and Brillouin linewidth**

685 Assume a least-squares fit of a model is applied to the normalized interferogram

686 to retrieve the Brillouin shift, Brillouin linewidth and elastic scatter ratio. Since

687 the variance of the normalized interferogram at each pixel is known by Eq. (A

688 10), the uncertainties in the least squares fitting parameters can be estimated.

689 To estimate these uncertainties, the covariance matrix (C) for the fitted

690 parameters can be computed using the weighted Jacobian, J. The diagonal of

691 the covariance matrix will contain the variances of the parameters.

$$C = (J^T J)^{-1} \tag{B 1}$$

692 The weighted Jacobian can be written as follows

$$J = \begin{pmatrix} \dfrac{\partial Q_1/\partial \nu_B}{\sqrt{\text{var } Q_1}} & \dfrac{\partial Q_1/\partial \Gamma_B}{\sqrt{\text{var } Q_1}} & \dfrac{\partial Q_1/\partial \gamma}{\sqrt{\text{var } Q_1}} \\ \vdots & \vdots & \vdots \\ \dfrac{\partial Q_P/\partial \nu_B}{\sqrt{\text{var } Q_P}} & \dfrac{\partial Q_P/\partial \Gamma_B}{\sqrt{\text{var } Q_P}} & \dfrac{\partial Q_P/\partial \gamma}{\sqrt{\text{var } Q_P}} \end{pmatrix} \tag{B 2}$$

693 With var Q_i given by Eq. (A 10) and

$$\partial Q_i / \partial \nu_B$$

$$= -2\pi \frac{\delta_i}{c} \frac{1}{1+\gamma} \exp\left(-\frac{\pi \Gamma_B \delta_i}{c}\right) \sin\left(\frac{2\pi \nu_B \delta_i}{c}\right) \cos\left(\frac{2\pi(\nu_L - \nu_0)\delta_i}{c}\right) \quad \text{(B 3)}$$

$$\partial Q_i / \partial \Gamma_B$$

$$= -\pi \frac{\delta_i}{c} \frac{1}{1+\gamma} \exp\left(-\frac{\pi \Gamma_B \delta_i}{c}\right) \cos\left(\frac{2\pi \nu_B \delta_i}{c}\right) \cos\left(\frac{2\pi(\nu_L - \nu_0)\delta_i}{c}\right) \quad \text{(B 4)}$$

$$\partial Q_i / \partial \gamma$$

$$= \frac{1}{(1+\gamma)^2} \Bigg(1$$

$$- \exp\left(-\frac{\pi \Gamma_B \delta_i}{c}\right) \cos\left(\frac{2\pi \nu_B \delta_i}{c}\right)\Bigg) \cos\left(\frac{2\pi(\nu_L - \nu_0)\delta_i}{c}\right) \quad \text{(B 5)}$$

694   δ_i is defined in (A 2). After solving the covariance matrix, the variances in

695   Brillouin shift and linewidth are along the diagonal and the covariance is in the

696   off-diagonal.

$$C = \begin{pmatrix} \Delta\nu_B{}^2 & \Delta\nu_B\Delta\Gamma_B \\ \Delta\nu_B\Delta\Gamma_B & \Delta\Gamma_B{}^2 \end{pmatrix} \quad \text{(B 6)}$$

697   The third row and column contain the covariance of the elastic scatter ratio,

698   but this parameter has no relationship to temperature and salinity and so is

699   omitted from (B 6) and ignored going forward.

700   **Appendix C: Propagation to variance in temperature, salinity, and**

701   **sound velocity**

702 Once the Brillouin linewidth and Brillouin shift are measured, the temperature

703 and salinity can be retrieved using an iterative process. Starting with an initial

704 guess and the measured Brillouin shift and linewidth, the temperature and

705 salinity are solved using the Gauss-Newton algorithm, implemented by

706 iterating on Eq. (C 1). $T_{k=0}$ and $S_{k=0}$ are the initial guesses and ν_B' and Γ_B' are

707 the measured Brillouin shift and Brillouin linewidth.

$$\begin{pmatrix} T_{k+1} \\ S_{k+1} \end{pmatrix} = \begin{pmatrix} T_k \\ S_k \end{pmatrix} + J'^{-1} \cdot \left[\begin{pmatrix} \nu_B' \\ \Gamma_B' \end{pmatrix} - \begin{pmatrix} \nu_B(T_k, S_k) \\ \Gamma_B(T_k, S_k) \end{pmatrix} \right] \qquad \text{(C 1)}$$

708 J' is a new Jacobian describing the sensitivities of the Brillouin shift and

709 linewidth to temperature and salinity.

$$J' = \begin{pmatrix} \partial \nu_B(T_k, S_k)/\partial T & \partial \nu_B(T_k, S_k)/\partial S \\ \partial \Gamma_B(T_k, S_k)/\partial T & \partial \Gamma_B(T_k, S_k)/\partial S \end{pmatrix} \qquad \text{(C 2)}$$

710 To determine the covariance in temperature and salinity, the Brillouin shift

711 and linewidth covariance matrix from Eq. (B 6) is transformed into a covariance

712 in temperature and salinity (C') using Jacobian J'.

$$C' = J'^{-1} C (J'^{-1})^T \qquad \text{(C 3)}$$

713 After solving the covariance matrix, the variances in temperature and

714 salinity are along the diagonal and the covariance is in the off-diagonal.

$$C' = \begin{pmatrix} \Delta T^2 & \Delta T \Delta S \\ \Delta T \Delta S & \Delta S^2 \end{pmatrix} \qquad \text{(C 4)}$$

The temperature and salinity covariance matrix can be converted to a random error in sound velocity using its sensitivities to those variables, by analogy with Eq. (C 3).

$$(\Delta V_s)^2 = (\partial V_s/\partial T \quad \partial V_s/\partial S) C' \begin{pmatrix} \partial V_s/\partial T \\ \partial V_s/\partial S \end{pmatrix} \tag{C 5}$$

Disclosures. The author declares no conflict of interest.

Data availability. No data were generated or analyzed in the presented research.

8. References

1. A. Popescu, K. Schorstein, and T. Walther, "A novel approach to a Brillouin–LIDAR for remote sensing of the ocean temperature," Appl. Phys. B 79, 955-961 (2004).

733   2. G. Hickman, J. Harding, M. Carnes, *et al.*, "Aircraft laser sensing of

734   sound velocity in water: Brillouin scattering," Remote Sens. of Environ.

735   36 (3), 165-178 (1991).

736   3. K. Liang, Y. Ma, J. Huang, *et al.*, "Precise measurement of Brillouin

737   scattering spectrum in the ocean using F–P etalon and ICCD," Applied

738   Physics B 105, 421-425 (2011).

739   4. Y. Emery and E. Fry, "Laboratory development of a LIDAR for

740   measurement of sound velocity in the ocean using Brillouin scattering,"

741   Ocean Optics XIII Vol. 2963, SPIE (1997).

742   5. Y. Ma, Y. Yu, H. Li, *et al.*, "Accurate measurement of high resolution

743   spectrum obtained by F–P etalon and ICCD," Appl. Phys. B 116, 575-

744   584 (2014).

745   6. K. Schorstein, E. Fry and T. Walther, "Depth-resolved temperature

746   measurements of water using the Brillouin lidar technique," Appl. Phys.

747   B 97, 931-934 (2009).

748   7. R. Dai, W. Gong, J. Xu, *et al.*, "The edge technique as used in Brillouin

749   lidar for remote sensing of the ocean," Appl. Phys. B 79, 245-248 (2004).

750   8. C. Englert, J. Harlander, D. Babcock, *et al.*, "Doppler asymmetric spatial

751   heterodyne spectroscopy (DASH): an innovative concept for measuring

752   winds in planetary atmospheres," Atmos. Opt. Modeling, Meas., and Sim.

753   II 6303, SPIE (2006).

754   9. C. Englert, D. Babcock, and J. Harlander, "Doppler asymmetric spatial

755   heterodyne spectroscopy (DASH): concept and experimental

756   demonstration," Appl. Opt. 46 (29), 7297-7307 (2007).

757   10. C. Englert, C. Brown, K. Marr, *et al.*, "As-built Specifications of

758   MIGHTI–The Thermospheric Wind and Temperature Instrument for the

759   NASA ICON Mission," Fourier Trans. Spect. (2016).

760   11. S. Burton, C. Hostetler, A. Cook, *et al.*, "Calibration of a high spectral

761   resolution lidar using a Michelson interferometer, with data examples

762   from ORACLES," Appl. Opt. 57 (21), 6061-6075 (2018).

763   12. S. Burton, R. Ferrare, C. Hostetler, *et al.*, "Second Generation Airborne

764   High Spectral Resolution Lidar (HSRL-2) Measurements of Various

765   Types of Aerosols During ORACLES, CAMP2EX, and ACTIVATE,"

766   Proc. AGU Fall Meeting, 2021AGUFM.A15C1650B (2021).

767   13. P. Sawamura, R. Moore, S. Burton, *et al.*, "HSRL-2 aerosol optical

768   measurements and microphysical retrievals vs. airborne in situ

769   measurements during DISCOVER-AQ 2013: an intercomparison study,"

770   Atmos. Chem. & Phys. 17 (11), 7229-7243 (2017).

771   14. D. Müller, C. Hostetler, R. Ferrare, *et al.*, "Airborne Multiwavelength

772   High Spectral Resolution Lidar (HSRL-2) observations during TCAP

773   2012: vertical profiles of optical and microphysical properties of a

774   smoke/urban haze plume over the northeastern coast of the US," Atmos.

775   Meas. Tech. 7 (10), 3487-3496 (2014).

15. J. Harlander and C. Englert, "Design of a real-fringe DASH interferometer for observations of thermospheric winds from a small satellite," Fourier Trans. Spect. FW1D.2 (2013).

16. X. Quan and E. Fry, "Empirical equation for the index of refraction of seawater," Appl. Opt. 34 (18), 3477-3480 (1995).

17. N. Fofonoff, R. Millard Jr., "Algorithms for the computation of fundamental properties of seawater," UNESCO Technical Papers in Marine Sciences 44 (1983).

18. J. Xu, X. Ren, W. Gong, *et al.*, "Measurement of the bulk viscosity of liquid by Brillouin scattering," Appl. Opt. 42 (33), 6704-6709 (2003).

19. M. Sharqawy, J. Lienhard, and S. Zubair, "Thermophysical properties of seawater: a review of existing correlations and data," Desalination & Water Treatment 16 (1-3), 354-380 (2010).

20. D. Bruneau and J. Pelon, "Simultaneous measurements of particle backscattering and extinction coefficients and wind velocity by lidar with a Mach–Zehnder interferometer: principle of operation and performance assessment," Appl. Opt. 42 (6), 1101-1114 (2003).

21. J. Churnside, "Review of profiling oceanographic lidar," Opt. Eng. 53 (5), 051405 (2014).

22. J. Harlander, "Algebraic ray trace analysis of spatial heterodyne spectrometers," Appl. Opt. 62 (16), 4288-4300 (2023).

797   23. D. Liu, J. Shi, X. Chen, *et al.*, "Brillouin lidar and related basic physics,"

798   Front. Phys. China 5, 82-106 (2010).

799   24. G. Scarcelli and S. Hyun Yun, "Multistage VIPA etalons for high-

800   extinction parallel Brillouin spectroscopy," Opt. Express 19 (11), 10913-

801   10922 (2011).

802   25. Z. Meng and V. Yakovlev, "Precise determination of Brillouin scattering

803   spectrum using a virtually imaged phase array (VIPA) spectrometer and

804   charge-coupled device (CCD) camera," Appl. Spect. 70 (8), 1356-1363

805   (2016).

806   26. Z. Coker, M. Troyanova-Wood, A. Traverso, *et al.*, "Assessing

807   performance of modern Brillouin spectrometers," Opt. Express 26 (3),

808   2400-2409 (2018).

809   27. C. Xie, P. Wang, C. Cai, *et al.*, "A Simple and accurate method for

810   Brillouin spectroscopy based on virtual imaging phased array

811   spectrometer and charge-coupled device cameras," Opt. Commun. 488,

812   126821 (2021).

813   28. I. Miller, LightMachinery, 80 Colonnade Road North, Unit #1, Ottawa,

814   ON K2E 7L2, Canada (personal communication, 2023).

815   29. J. Hair, C. Hostetler, Y. Hu, *et al.*, "Combined atmospheric and ocean

816   profiling from an airborne high spectral resolution lidar," EPJ Web of

817   Conferences 119 EDP Sciences (2016).

818   30. Y. Zhou, W. Chen, D. Liu, *et al.*, "Multiple scattering effects on the

819   return spectrum of oceanic high-spectral-resolution lidar," Opt. Express

820   27 (21), 30204-30216 (2019).

821   31. W. Brown, O. Schofield, S. Glenn, *et al.*, "Mid-Atlantic Bight cold pool

822   based on ocean glider observations," Cont. Shelf Res. 264, 105040

823   (2023).

824   32. E. Fry, Y. Emery, X. Quan, *et al.*, "Accuracy limitations on Brillouin

825   lidar measurements of temperature and sound speed in the ocean," Appl.

826   Opt. 36 (27), 6887-6894 (1997).

827   33. B. Joelson and G. Kattawar, "Multiple scattering effects on the remote

828   sensing of the speed of sound in the ocean by Brillouin scattering," Appl.

829   Opt. 35 (15), 2693-2701 (1996).

830   34. B. Garau, S. Ruiz, W. Zhang, *et al.*, "Thermal lag correction on Slocum

831   CTD glider data," J. Atmos. Ocean. Technol. 28 (9), 1065-1071 (2011).

832   35. Y. Wang, C. Luo, S. Yang, *et al.*, "Modified thermal lag correction of

833   CTD data from underwater gliders," J. Coast. Res. 99 (sp1), 137-143

834   (2020).

835   36. X. Lu, Y. Hu, Y. Yang, *et al.*, "Antarctic spring ice-edge blooms

836   observed from space by ICESat-2," Remote Sens. Environ. 245, 111827

837   (2020).

838   37. Z. Chen and E. Curchitser, "Interannual Variability of the Mid-Atlantic

839   Bight Cold Pool," J. Geophys. Res. Oceans 125 (8), e2020JC016445

840   (2020).

841   38. G. Seroka, T. Miles, Y. Xu, *et al.*, "Rapid shelf-wide cooling response of

842   a stratified coastal ocean to hurricanes," J. Geophys. Res. Oceans 122 (6),

843   4845-4867 (2017).

844   39. H. du Pontavice, T. Miller, B. Stock, *et al.*, "Ocean model-based

845   covariates improve a marine fish stock assessment when observations are

846   limited," ICES J. Mar. Sci. 79 (4), 1259-1273 (2022).

847   40. S. Glenn, T. Miles, G. Seroka, *et al.*, "Stratified coastal ocean interactions

848   with tropical cyclones," Nat. Commun. 7 (1), 10887 (2016).

849   41. T. Miles, S. Glenn, J. Kohut, *et al.*, "Observations of Hurricane Sandy

850   from a glider mounted aquadopp profiler," Proc. 2013 OCEANS-San

851   Diego IEEE (2013).

852   42. E. Regnier, "Public evacuation decisions and hurricane track

853   uncertainty," Manag. Sci. 54 (1), 16-28 (2008).

854   43. K. Friedland, T. Miles, A. Goode, *et al.*, "The Middle Atlantic Bight Cold

855   Pool is warming and shrinking: Indices from in situ autumn seafloor

856   temperatures," Fish. Oceanogr. 31 (2), 217-223 (2022).

857   44. T. Miles, S. Murphy, J. Kohut, *et al.*, "Offshore wind energy and the Mid-

858   Atlantic Cold Pool: A review of potential interactions," Mar. Technol.

859   Soc. J. 55 (4), 72-87 (2021).

860   45. A. López, J. Wilkin, and J. Levin, "Doppio–a ROMS (v3. 6)-based

861   circulation model for the Mid-Atlantic Bight and Gulf of Maine:

862   configuration and comparison to integrated coastal observing network

863   observations," Geosci. Model Dev. 13 (8), 3709-3729 (2020).

864   46. K. Koutantou, P. Brunner, and J. Vazquez-Cuervo, "Validation of NASA

865   Sea Surface Temperature Satellite Products Using Saildrone Data," Rem.

866   Sens. 15 (9), 2277 (2023).

867   47. R. Weisberg, A. Barth, A. Alvera-Azcárate, *et al.*, "A coordinated coastal

868   ocean observing and modeling system for the West Florida Continental

869   Shelf," Harmful Algae 8 (4), 585-597 (2009).